JOURNAL OF GUIDANCE, CONTROL, AND DYNAMICS
Vol. 21, No. 4, July–August 1998

Interplanetary Spacecraft Controllers Using Thrusters

Hari B. Hablani*
The Boeing Company, Downey, California 90241

Design of attitude controllers for interplanetary spacecraft is addressed. The first controller is for Rhumb-line precession using an almost periodic train of thruster pulses at a constant phase with the sun. Earlier relationships are expanded and interlaced coherently and demonstrated on a Mercator plot. The second controller is for nutation damping. For spacecraft with products of inertia, a control scheme is formulated that involves four phase angles, 90 deg apart in a nutation cycle, where the positive or negative control impulses about the transverse axes are injected to damp the nutations. The third controller is for attitude control during aerobraking for planetary orbit insertion. The controller seeks and maintains a zero aerodynamic torque orientation. Because this orientation may correspond to a constant bias angle of attack measured from the instantaneous velocity vector turning at a nonuniform pitch rate, a pitch angular acceleration command profile is developed for parameterizing a thruster controller. The fourth, and last, controller is for soft landing. It comprises a longitudinal velocity controller enhanced by gravity turn and a constant velocity phase at low altitudes near ground, a lateral velocity controller producing commands to pitch spacecraft at varying rates, and a reaction jet controller for tracking the commanded pitch angle and rate until touchdown. Satisfactory performance of all controllers is amply demonstrated.

I. Introduction

THIS paper describes various controllers for interplanetary spacecraft such as Mars Environment Surveyor, Mars Global Surveyor (MGS), Mars Surveyor Program, and Mars Surface Exploration Pre-Project. The paper deals with both spin-stabilized and three-axis-stabilized spacecraft, and it consists of four main sections. Section II describes a technique for designing a Rhumb-line precession controller using an almost periodic train of thruster pulses at a constant phase with the sun. The relationships from different sources in the literature are expanded, coherently interwoven, and illustrated with a detailed, realistic simulation of large-angle precession dynamics of a proposed interplanetary spacecraft (MGS). A Rhumb-line precession, along with its ungrowing nutation loops, is demonstrated on a Mercator plot. Because the precession of a momentum vector inevitably is accompanied by nutations, these high-frequency oscillations at the end of precession must be damped for satisfactory pointing accuracy of the spin axis.

A control scheme is devised and illustrated for this purpose in Sec. III. A spinning spacecraft with products of inertia exhibits constant biases in its transverse angular rates. To effect nutation damping of such spacecraft, a control scheme is taken up from the literature and honed. The scheme involves, inter alia, bandpass filters to eliminate biases from the transverse rates. Four phase angles, 90 deg apart in a nutation cycle, are determined analytically, where positive or negative control impulses about a transverse axis are fired for nutation damping. It is shown that when a spacecraft has small products of inertia, the final steady-state nutation angle equals the angle between the geometric spin axis and the adjacent principal axis.

Section IV presents an attitude controller, using thrusters, for the aerobraking phase of Mars orbit insertion. As a spacecraft approaches its destination planet, it is despun and its velocity is reduced to establish a planetary orbit. The apoapsis of this highly elliptic orbit is brought closer to the planet by aerobraking instead of using propellant for velocity reduction. For a portion of the orbit near periapsis, where aerobraking is effective, an attitude controller is designed to seek and maintain a zero aerodynamic torque orientation of the spacecraft. In the present application, this orientation corresponds to a constant, positive bias angle of attack measured from the instantaneous velocity vector. Because, in an elliptic orbit, this vector turns at a nonuniform pitch rate, a pitch angular acceleration command profile is developed and the parameters for integral pulse frequency modulation (IPFM) thruster controller are determined for tracking time-varying orientations.

Section V presents a soft-landing controller for the Mars Lander. It comprises 1) a longitudinal velocity controller employing a velocity–altitude reference trajectory for guidance, a gravity turn below 45 m, and a constant-velocity phase below 5-m altitude until a soft impact is sensed by the navigation system; 2) a lateral velocity controller that requires pitching the spacecraft first at a rate inversely proportional to the current slant range and then according to gravity turn activated at a suitable low altitude; and 3) an IPFM reaction jet controller for tracking the commanded pitch angle and rate profile until touchdown. A radar altimeter is used until the spacecraft descends to a 45-m altitude. Afterward, an inertial reference unit, inheriting the errors of the radar altimeter at 45 m, is used for landing. The optimum gains for both longitudinal and lateral controllers are determined, and first-order digital fading memory filters are used, the coefficients of which are optimized with stochastic response analysis to smooth noisy measurements.

Ample numerical results, within the space allowed, are presented to demonstrate effectiveness of all controllers. The relationship of the present work to the previous work is identified in each section below.

II. Rhumb-Line Precession of Spin-Stabilized Spacecraft

The spin axis of a spacecraft can be precessed along either a great arc or a Rhumb line between the initial orientation and the final orientation of a spacecraft in a celestial sphere.[1] In the former case the phase angle of the thruster firing varies significantly with each spin cycle, leading to operational complexities, whereas in the latter case the phase angle is constant, easily controlled by a sun sensor. Rhumb-line precessions are therefore more common than great-arc precessions.

A. Analysis

Figure 1 depicts the geometry of spin-axis precession produced by thrusters. Let $x_b y_b z_b$ be the spacecraft-fixed frame, with z_b as the spin axis of the spacecraft. The precession torque $F\ell$ (F = force, ℓ = moment arm) is generated about an axis forming an angle β with the transverse axis x_b. The spin angle of the spacecraft is denoted ϕ and is measured from the ascending node line x_b' as shown in Fig. 1. Let t_w denote the short pulsewidth (20–200 ms) of the thrusters. The angular momentum imparted by each pulse is then $F\ell t_w$ and the precession angle $\mathrm{d}P$ about an axis transverse to both torque axis and spin axis is (see Fig. 1) $\mathrm{d}P = F\ell t_w/(I_3\omega_s)$, where

Received Jan. 31, 1997; revision received Jan. 29, 1998; accepted for publication Jan. 29, 1998.

*Principal Engineering Specialist, Avionics and Software Group, Advanced Programs, Space Systems Division. Associate Fellow AIAA.

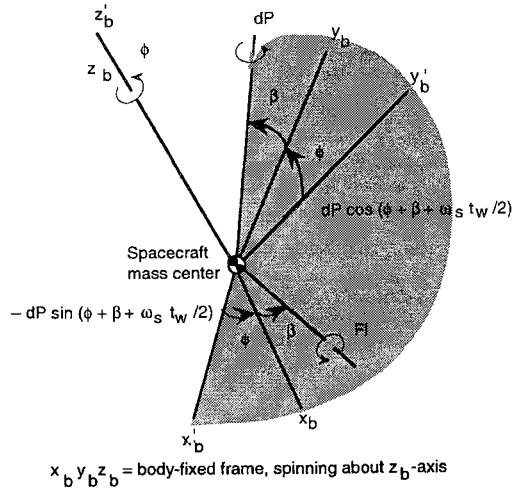

Fig. 1 Geometry of precession of spin axis produced by thrusters.

I_3 is the spacecraft moment of inertia about the spin axis and ω_s is the spin rate. The phase angle of the center of the thruster firing, measured from the axis x_b' is $\phi_\beta = (\phi_0 + \beta + \omega_s t_w/2)$, where ϕ_0 is the spin angle ϕ at which thrusters turn on instantaneously for t_w seconds for precessing the spacecraft. The components of dP in the frame $\mathcal{F}^{b'}: x_b' y_b' z_b'$ ($z_b' = z_b$) are $[-dP \sin\phi_\beta \;\; dP \cos\phi_\beta \;\; 0]^{\mathcal{F}^{b'}}$, the component about the spin axis being zero by definition. To relate these components with the changes in longitude and colatitude (declination) of the spin axis z_b in an inertial frame, let ψ denote the spin-axis longitude about the inertial axis Z_1, measured from an inertially fixed axis X_1, and θ denote its colatitude about the ascending node line x_b'. Small changes $d\psi$ in longitude and $d\theta$ in colatitude then will have these components in the $x_b' y_b' z_b'$ frame: $[d\theta \;\; d\psi \sin\theta \;\; d\psi \cos\theta]^{\mathcal{F}^{b'}}$, where the spin-axis component is now nonzero, implying that, notwithstanding earlier inference, the spin angle does change slightly with each firing, varying the spin period as a consequence. In view of this, the requirement that the phase angle ϕ_β be constant for all firings will be satisfied only by monitoring this angle; clearly, firings will not take place exactly at the same spin-period interval. Focusing on the equality of x_b' and y_b' components of the two vectors ($d\theta = -dP \sin\phi_\beta$, $d\psi \sin\theta = dP \cos\phi_\beta$), we divide x_b' components by y_b' components and obtain

$$\frac{d\theta}{\sin\theta} = -d\psi \tan\phi_\beta \tag{1}$$

Because the angle ϕ_β is controlled so that it is the same for all firings with a sun sensor within its measurement accuracies, the integration of Eq. (1) leads to

$$-\log_e \tan\tfrac{1}{2}\theta = \psi \tan\phi_\beta + \text{const} \tag{2}$$

With the longitude ψ as abscissa and $(-\log_e \tan\frac{1}{2}\theta)$ as ordinate—the coordinates of a Mercator plot—and the angle ϕ_β as slope, Eq. (2) is a straight-line equation, confirming that this is indeed a Rhumb-line maneuver. Invoking the initial and the final values θ_1, θ_2 of colatitude and ψ_1, ψ_2 of longitude, Eq. (2) yields the following desired equation:

$$-\tan\phi_\beta = \frac{1}{\psi_2 - \psi_1} \log_e \frac{\tan\frac{1}{2}\theta_2}{\tan\frac{1}{2}\theta_1} \tag{3}$$

which can be used to determine the phase angle ϕ_β. For an agreement between Eq. (3) and Eq. (1) of Ref. 1, observe that the ascending node line x_b' is typically due east (the solar sensor emitting maximum output) and therefore the phase angle ϕ_β is sometimes called a heading angle. Rhumb angle, denoted Φ, is measured from either local north or local south, and is called, accordingly, Φ_N or Φ_S. One then has $\phi_\beta = \pi/2 + \Phi_N$ or $\phi_\beta = -\pi/2 + \Phi_S$. Substituting these equations in the left side of Eq. (3), one arrives at Eq. (1) of Ref. 1 or Eq. (30) of Ref. 2. The two values of ϕ_β are in line with Eq. (32) of Ref. 2.

The total change in the colatitude angle θ is obtained by integrating the equation $d\theta = -dP \sin\phi_\beta$, yielding

$$(\theta_2 - \theta_1) = \{-P \cos\Phi_N \quad \text{or} \quad P \cos\Phi_S\} \tag{4}$$

where P is the total precession angle effected by N firings arrived at by summing up all dP for N firings:

$$P = \frac{NF\ell t_w}{I_3 \omega_s} \tag{5}$$

Whereas colatitudes θ_1 and θ_2 are dictated by the mission and spacecraft–sun geometry, the phase angle ϕ_β is calculated from Eq. (3) and Φ_N or Φ_S from $\Phi_N = \phi_\beta - \pi/2$, $\Phi_S = \phi_\beta + \pi/2$; Eq. (4) then yields the required precession angle P, and Eq. (5) the required number N of firings

$$N = \left| \frac{\theta_2 - \theta_1}{\cos\Phi} \frac{I_3 \omega_s}{F\ell t_w} \right| \tag{6}$$

where $\Phi = \Phi_N$ or Φ_S. When the pulsewidth t_w is not small (that is, the condition $\omega_s t_w/2 \ll 1$ is not satisfied), a more accurate version of Eq. (6), presented in the unabridged version of this paper,[3] is used. Equation (6) must be integerized to its nearest integer to minimize deviation of the actual, final longitude and colatitude from the desired values ψ_2 and θ_2. Moreover, to assess the fuel efficiency of a Rhumb-line precession, one may compare numerically the precession angle P, Eq. (5), with the great arc length Γ between the initial and the final latitudes and longitudes

$$\Gamma = \cos^{-1}[\cos\theta_1 \cos\theta_2 + \sin\theta_1 \sin\theta_2 \cos(\psi_2 - \psi_1)] \tag{7}$$

As stated earlier, the phase angle ϕ_β is required to be the same for each thruster firing. Because the phase angle or, equivalently, ϕ_0 (ϕ at $t = 0$), is measured from the ascending node line x_b', whose orientation angle ψ varies slowly with each thruster firing, the spin angle ϕ does not cross the value ϕ_0 at a uniform spin-period interval. Consequently, a sun sensor must be used to ensure that the spin angle ϕ equals ϕ_β for each thruster firing. Finally, a comment about the nutations of the spacecraft while precessing: Typically, the spin period of a spacecraft is an irrational multiple of the nutation period and therefore the nutation amplitude does not grow monotonically with thruster firings; instead, it waxes and wanes and is self-limited.

B. Illustration

Six first-order equations governing dynamics and inertial orientation of a spinning spacecraft are simulated. Table 1 in Ref. 3 furnishes the parameters used for simulating a Rhumb-line precession illustrated conceptually in Figs. 19.7 and 19.8 of Wertz.[4] The control torque is produced by two z thrusters located diametrically opposite on the rim of the spacecraft, firing oppositely. Figure 2 shows a dashed Rhumb line (not clearly visible) joining the initial and the final specified locations of the spin axis on a Mercator plot. Because the Rhumb-line length P is 75.5 deg whereas the corresponding great circle arc Γ is 59 deg, this Rhumb-line precession is inefficient compared with the great-circle precession. The advantage, nonetheless, of the Rhumb-line precession is the constancy of the phase angle ϕ_0, equal to 31.71 deg in this example, within ±0.25-deg measurement accuracy of the sun sensor. Figure 2 illustrates, in addition, the undulations of the nutation loops accompanying the precession; their amplitudes do not grow unremittingly because the nutation period, 27.33 s, is not an integer multiple of the spin period, 20 s. The corresponding nutation angle of the spacecraft, denoted γ and defined as

$$\gamma = \frac{\left[(I_1\omega_1)^2 + (I_2\omega_2)^2\right]^{\frac{1}{2}}}{I_3 \omega_3} \tag{8}$$

varies discontinuously with each firing, remaining constant in the interim. Numerical results show that the angle γ is within 0.4 deg and does not increase. The longitude ψ and the colatitude θ vary with time, starting from their initial values and reaching their final desired values at the end of precession in 5630 s, remaining essentially constant afterward—essentially because the spacecraft continues to

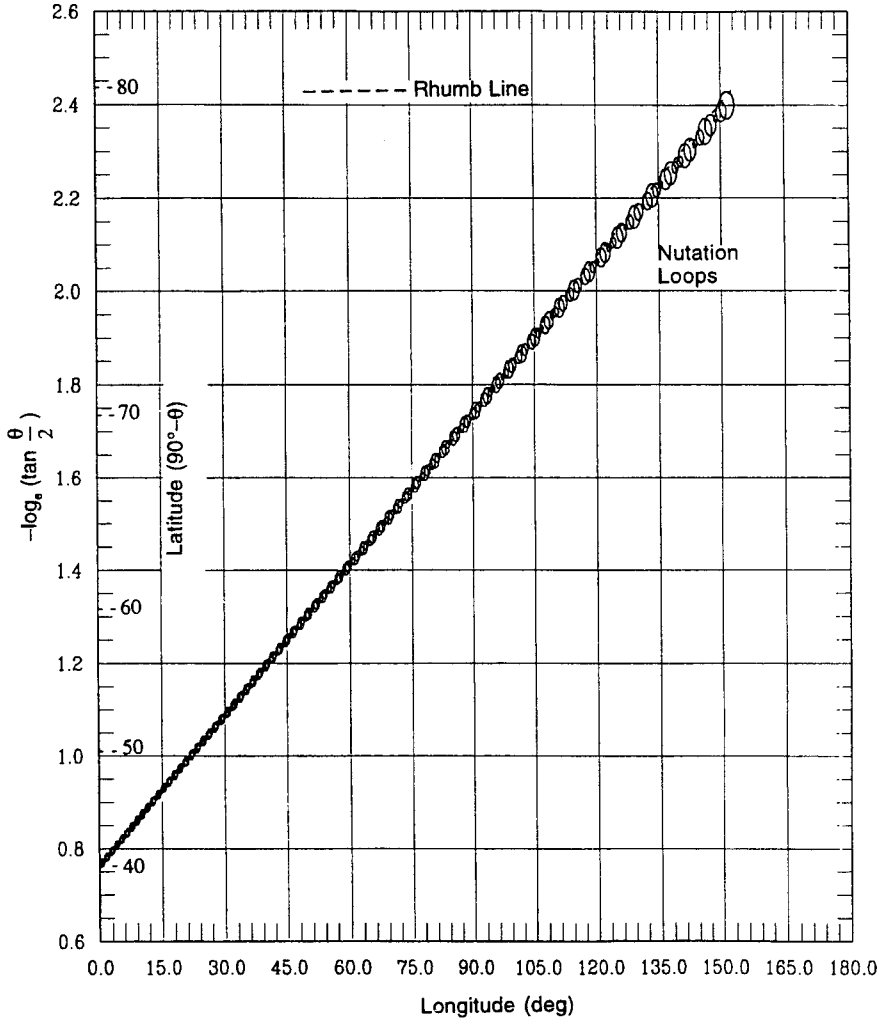

Fig. 2 Rhumb-line precession of a spin-stabilized spacecraft: latitude vs longitude (Mercator projection).

nutate with some residual amplitude after precession, indicating the need for active or passive nutation damping.

III. Active Nutation Damping

This section is concerned with spacecraft with zero and yz products of inertia and is based on Ref. 5. Although Ref. 5 assumes that the spacecraft spins about the minor axis, the following analysis is for the major spin axis. Hence, according to the definition of the body-fixed frame $x_b y_b z_b$ in Fig. 1, $I_3 > I_2 \geq I_1$.

A. Control Strategy

Consider the equations of motion governing the transverse rates ω_1 and ω_2, influenced by the unspecified control torques N_1 and N_2 for nutation damping. Following Devey et al.,[5] define quasinutation frequencies

$$\omega_{n1} = \frac{(I_3 - I_2)\omega_s}{I_1} \tag{9a}$$

$$\omega_{n2} = \frac{(I_3 - I_1)\omega_s}{I_2} \tag{9b}$$

$$\omega_n = \sqrt{\omega_{n1}\omega_{n2}} \tag{9c}$$

Assuming that the transverse rates $|\omega_j| \ll \omega_s$ $(j = 1, 2)$, the spin speed ω_3 remains essentially constant: $\omega_3 \approx \omega_s$. The free response, therefore, of the two equations of motion governing transverse angular rates can be written as

$$\omega_1 + jk\omega_2 = \rho_0 \exp j(\theta_0 + \alpha) \tag{10}$$

where $j^2 = -1$, $k = \sqrt{(\omega_{n1}/\omega_{n2})}$, $\alpha = \omega_n(t - t_0)$, and ρ_0 and θ_0 are initial amplitude and phase of the motion $\omega_1(t)$ and $\omega_2(t)$ at $t = t_0$:

$$\rho_0 \triangleq \left(\omega_{10}^2 + k^2\omega_{20}^2\right)^{\frac{1}{2}} \tag{11a}$$

$$\theta_0 \triangleq \tan^{-1}(k\omega_{20}, \omega_{10}) \tag{11b}$$

Further, Ref. 3 shows that, for nutation damping with the control torque N_1 about the x axis, the x-angular impulses imparted by the thrusters must be

$$@\ \theta_0 = -\frac{\alpha}{2} : N_1\Delta t = \frac{-k_c I_1 \rho_0(\alpha/2)}{\sin(\alpha/2)} \tag{12a}$$

$$@\ \theta_0 = \pi - \frac{\alpha}{2} : N_1\Delta t = \frac{k_c I_1 \rho_0(\alpha/2)}{\sin(\alpha/2)} \tag{12b}$$

where $\Delta t = t - t_0$ is selected such that Eqs. (12) are satisfied for a small k_c; $k_c = 0.05$, for example. For y thrusters, the angular impulses for nutation damping are found to be

$$@\ \theta_0 = \frac{\pi}{2} - \frac{\alpha}{2} : N_2\Delta t = \frac{-k_c I_2 \rho_0(\alpha/2)}{\sin(\alpha/2)} \tag{13a}$$

$$@\ \theta_0 = -\frac{\pi}{2} - \frac{\alpha}{2} : N_2\Delta t = \frac{k_c I_2 \rho_0(\alpha/2)}{\sin(\alpha/2)} \tag{13b}$$

For detailed derivation, see Ref. 3.

B. Spacecraft with Product-of-Inertia I_{23}

Here, we assume that only $I_{23} = -\int yz\, dm$ product of inertia is nonzero. Because the products of inertia are typically much smaller

than the moments of inertia, it is beneficial, for analytical ease, to treat each product of inertia separately. The following analysis therefore can be retraced for I_{12} and I_{31} products of inertia individually, though we do not attempt that here. We also point out that the above definition of I_{23} includes the negative sign, unlike the convention used by Devey et al.[5]

Proceeding with the vector equation of motion of a rigid body, with I_{23} in the inertia matrix, three scalar equations are derived for zero external torque acting on the spacecraft. We then invoke typical and presently legitimate assumptions that $|\omega_j| \ll |\omega_3|$ for $j = 1, 2$; $|I_{23}| \ll (I_1, I_2, I_3)$; and $\omega_3 \approx \omega_s$, where ω_s = a constant spin speed. The transverse equation governing ω_1 possesses a forcing term due to the product-of-inertia I_{23}. Denote this by μ and introduce a nondimensional product-of-inertia parameter f as follows:

$$\mu \triangleq \frac{\omega_s^2 I_{23}}{I_1} \tag{14a}$$

$$f \triangleq I_{23}^2/(I_2 I_3) \tag{14b}$$

The product of inertia alters the nutation frequency ω_n, Eq. (9c), to

$$\omega_n'^2 = \frac{\omega_{n1}(\omega_{n2} + f\omega_s)}{1 - f} \tag{15}$$

The transverse rates obtained by solving the transverse equations exhibit the following forced response:

$$\omega_1 = (\mu/\omega_n')\sin\omega_n' t \tag{16a}$$

$$\omega_2 = (\mu/\omega_{n1})(1 - \cos\omega_n' t) \tag{16b}$$

from which we conclude that the transverse rate ω_2, after nutation damping, will settle on its bias value $\omega_{2b} = \mu/\omega_{n1}$. As one would anticipate, ω_{2b} is related to the tilt angle λ, about the geometric axis x_b, between the orthogonal axes $y_b z_b$ and the principal axes $y_p z_p$. In particular, it can be shown that, for small tilt angle, $|\lambda| \ll 1$, the moments-of-inertia I_2 and I_3 are essentially the principal values and $I_{23} \approx (I_2 - I_3)\lambda$, which indicates that, in the present application, because $I_3 > I_2$, the product-of-inertia I_{23} and the tilt angle λ have opposite signs. With the aid of Eqs. (9a) and (14a), the bias rate ω_{2b} is found to be equal to $-\lambda\omega_s$, matching with Eq. (39) of Ref. 5 except for the negative sign arising from the difference that Ref. 5 deals with spin about the minimum moment of inertia and this paper is dealing with spin about the maximum moment-of-inertia.

Let $\boldsymbol{b}_1, \boldsymbol{b}_2, \boldsymbol{b}_3$ be the unit vectors along the geometric, spacecraft-attached frame $x_b y_b z_b$. We then observe that the steady-state spin rate of the spacecraft, $\boldsymbol{\omega}$, equals $\omega_{2b}\boldsymbol{b}_2 + \omega_s\boldsymbol{b}_3$ because, in the principal frame $x_p y_p z_p$ (with $\boldsymbol{p}_3$ as the unit vector along the principal spin-axis z_p), in view of the relationship $\omega_{2b} = -\lambda\omega_s$, the angular velocity $\boldsymbol{\omega}$ equals $(\omega_s - \lambda\omega_{2b})\boldsymbol{p}_3$, which induces no angular motion about the transverse principal axes x_p and y_p. In the absence of nutation, the steady-state angular momentum $\boldsymbol{h}$ of the spacecraft in the $x_b y_b z_b$ frame is

$$\boldsymbol{h} = (I_2\omega_{2b} + I_{23}\omega_s)\boldsymbol{b}_2 + (I_3\omega_s + I_{23}\omega_{2b})\boldsymbol{b}_3 \tag{17}$$

Substituting $\omega_{2b} = -\lambda\omega_s$, $I_{23} \approx (I_2 - I_3)\lambda$ and ignoring the λ^2 term, $\boldsymbol{h}$ simplifies to

$$\boldsymbol{h} \approx -\lambda I_3\omega_s\boldsymbol{b}_2 + I_3\omega_s\boldsymbol{b}_3 \tag{18}$$

The corresponding steady-state nutation angle γ, defined by Eq. (8), is thus $\gamma = |\lambda|$. The steady-state values $\omega_{2b} = -\lambda\omega_s$ and $\gamma = |\lambda|$ help verify the numerical results.

To implement the nutation damping strategies (12) and (13), the phase angle θ_0 must be determined. For the zero product-of-inertia case, this is accomplished using the definition (11b), wherein the unbiased transverse rates are sensed by gyros. A nonzero product of inertia, however, renders this procedure inadequate because gyros measure transverse rates containing biases. Therefore, the bias ω_{2b}, determined above, and ω_{1b}, if it exists due to the product-of-inertia I_{13} not considered here, must be filtered out from ω_1 and ω_2 sensed by the gyros. This filtering is performed with a bandpass filter, one for each axis.

C. Bandpass Filters

The transfer function of a bandpass filter is

$$H_{BP}(s) = \frac{2\zeta\omega_n s}{s^2 + 2\zeta\omega_n s + \omega_n^2} \tag{19}$$

centered at the nutation frequency ω_n; here, s is the Laplace variable and ζ is a suitable damping factor. Because this filter is used as a part of a sampled control system, its following discrete form is derived:

$$H_{BP}(z) = \frac{b_0 - b_0 z^{-2}}{1 - a_1 z^{-1} - a_2 z^{-2}} \tag{20}$$

where z is the discrete transform and the polynomial coefficients are defined in Ref. 3 in terms of the semisample angle $\delta_m = \omega_m t_s/2$, with $\omega_m = (2/t_s)\tan(\omega_n t_s/2)$ and t_s equals the sample period. Let $\omega_{2,k}$ denote the kth sample of the input angular rate ω_2 at $t = t_k$, and $\omega_{2f,k}$ denote the kth output sample. Furthermore, in the present application and typically, the angle δ_m is much less than unity and therefore $\delta_m^{-1} \gg 1$. Using this assumption, a simplified time-domain version of Eq. (20) is then[3]

$$\omega_{2f,k} = 2\omega_{2f,k-1} - \omega_{2f,k-2} + \zeta\omega_m t_s(\omega_{2,k} - \omega_{2,k-2}) \tag{21}$$

By using the discrete time-domain version (21), we avert the need for the derivative $\dot{\omega}_2$ of the angular rate ω_2 in the continuous time-domain version of Eq. (19). This is a significant benefit because the acceleration $\dot{\omega}_2$ is not measured.

D. Numerical Results

For results concerning zero product of inertia, see Ref. 3. Figure 3 illustrates nutation damping when the product-of-inertia parameter f is 0.01. The corresponding tilt angle λ between the geometric spin-axis z_b and the principal axis z_p is -10.3 deg and the bias rate $\omega_{2b} = -\lambda\omega_s$ equals 3.24 deg/s. The filtered rate ω_{2f} is obtained by using the time-domain discrete Eq. (21) with ζ equal to 0.2. The corresponding time delay for the filter output ω_{2f} to rise to its steady-state amplitude is nearly two nutation periods (54.7 s). Moreover, owing to the product-of-inertia I_{23}, the nutation angle γ, defined by

$$\gamma = \frac{(h_{b1}^2 + h_{b2}^2)^{\frac{1}{2}}}{h_{b3}} \tag{22}$$

is not constant now. To damp the nutations, the control policy, Eq. (13), is invoked after ω_{2f} attains its steady state. As damping progresses, the nutation angle γ (Fig. 4) approaches the magnitude of the tilt angle, $|\lambda| = 10.3$ deg. At the end of nutation damping,

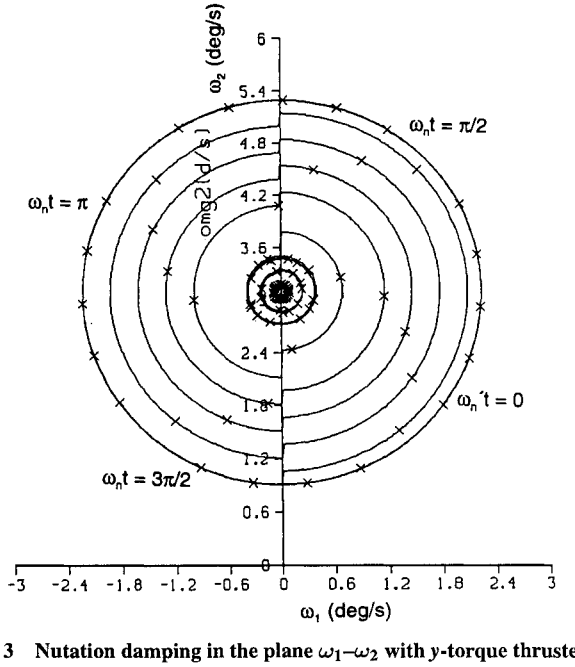

Fig. 3 Nutation damping in the plane ω_1–ω_2 with y-torque thrusters.

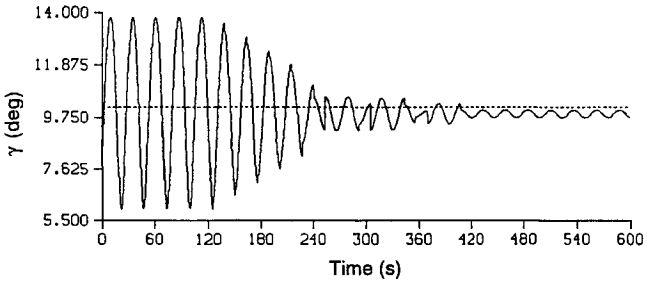

Fig. 4 Nutation angle γ vs time.

while the filtered rate ω_{2f} nears zero, ω_2 oscillates with a small amplitude (see Fig. 3) over the bias rate $\omega_{2b} = 3.24$ deg/s.

IV. Thruster Attitude Control During Aerobraking

Real spacecraft are seldom symmetric and streamlined and therefore atmospheric drag generates a torque that must be nullified to keep the spacecraft stable.[6,7] Aerodynamics of the aerobraking configuration of the spacecraft at hand reveals that the pitch torque coefficient—the only coefficient required in this study—is zero for a positive angle-of-attack $\alpha_{\text{atk},b}$ equal to 3.15 deg and, for aerodynamic stability or equivalently for positive pitch stiffness at angle-of-attack α_{atk} equal to zero, the slope of this coefficient near the equilibrium angle $\alpha_{\text{atk},b}$ is negative, as desired. To null the aerodynamic torque acting on the spacecraft, α_{atk} must be commanded to be equal to the equilibrium angle $\alpha_{\text{atk},b}$.

A. Analysis

Figure 5 depicts the geometric relationship between the angle-of-attack α_{atk}, pitch angle α_2, and the angle ξ between the velocity vector $\boldsymbol{v}$ and the local horizontal $\boldsymbol{O}_1$ in the orbit plane. The local vertical local horizontal orbit triad $\boldsymbol{O}_1, \boldsymbol{O}_2, \boldsymbol{O}_3$ and the spacecraft attached triad $\boldsymbol{b}_1, \boldsymbol{b}_2, \boldsymbol{b}_3$ shown in Fig. 5 are defined as usual. Because the nose of the spacecraft is along $\boldsymbol{b}_1$, the angle of attack is, by definition, $\alpha_{\text{atk}} = \alpha_2 - \xi$. The angle ξ varies with the spacecraft true anomaly θ measured from the periapsis or with η measured from the line of ascending node (Fig. 5), and the objective of the pitch controller is to ensure that $\alpha_{\text{atk}} = \alpha_{\text{atk},b}$, that is, to keep the pitch angle α_2 equal to the commanded pitch angle α_{2c} where $\alpha_{2c} = \alpha_{\text{atk},b} + \xi$, and ξ varying with the true anomaly θ thus

$$\tan\xi = \frac{e\sin\theta}{1 + e\cos\theta} \tag{23}$$

where e is the eccentricity of the orbit.

To design a reaction jet controller for tracking a varying α_{2c}, corresponding inertial pitch acceleration command is determined, for it governs the minimum control torque required. The inertial pitch rate command ω_{2c} in terms of the pitch rate command $\dot{\alpha}_{2c}$ and the true anomaly rate $\dot{\theta}$ is $\omega_{2c} = \dot{\alpha}_{2c} - \dot{\theta} = \dot{\xi} - \dot{\theta}$. Differentiation of Eq. (23) then leads to

$$\omega_{2c} = -\frac{\dot{\theta}(1 + e\cos\theta)}{1 + e^2 + 2e\cos\theta} \tag{24}$$

a further differentiation of which yields the sought inertial pitch acceleration command $\dot{\omega}_{2c}$

$$\dot{\omega}_{2c} = \frac{\dot{\theta}^2 e\sin\theta(1 + 3e^2 + 4e\cos\theta)}{(1 + e^2 + 2e\cos\theta)^2} \tag{25}$$

With the pitch command α_{2c} and the inertial pitch-rate command ω_{2c}, the angle of attack is commanded to be equal to the constant bias angle $\alpha_{\text{atk},b}$. The actual angle of attack, of course, will depend on the performance of the IPFM reaction jet controller used here.[8]

B. Numerical Results

In the initial phase of aerobraking, the altitude of periapsis h_p, and of apoapsis h_a, are $h_p = 105$ km and $h_a = 33{,}264$ km, whereas in the final phase the apoapsis altitude decreases to $h_a = 768$ km. In the initial phase, the atmospheric torque (Fig. 6) caused by the roll and yaw drag forces is significant for nearly 10 min centered around the periapsis. In the final phase, this duration expands to 20 min.

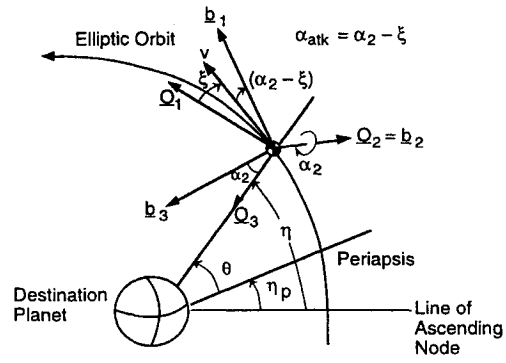

Fig. 5 Attitude geometry of spacecraft for aerobraking in an elliptic orbit.

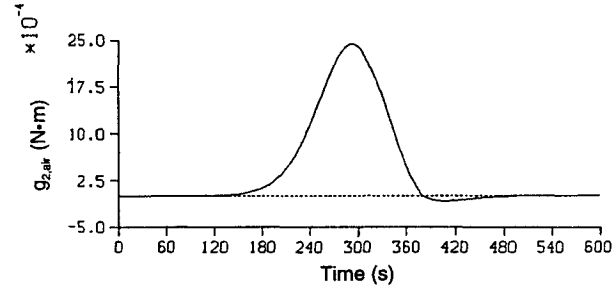

Fig. 6 Pitch atmospheric torque ($g_{2,\text{air}}$) near periapsis of the initial aerobraking orbit.

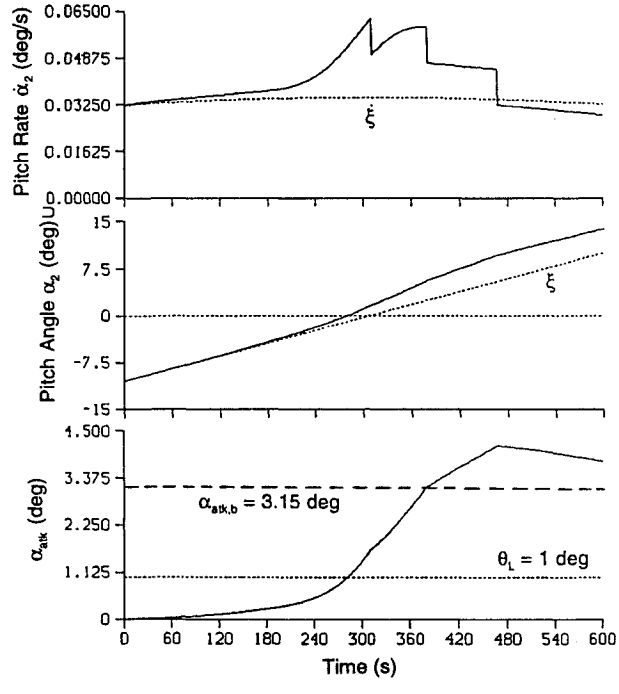

Fig. 7 Tracking a bias angle of attack: angle of attack, pitch, and pitch rate vs time.

Figure 11 of Ref. 3, displaying $\dot{\omega}_{2c}$ pertaining to the initial aerobraking altitudes, indicates that the maximum commanded torque will be: pitch inertia $* \dot{\omega}_{2c,\max} = 1.43e{-}4$ N · m. The actual thruster torque, however, is four orders of magnitude larger: 4.52 N · m. To mitigate the impact of this disparity, thrusters are turned on for only 20 ms, imparting a pitch angular momentum of 0.09 N · m or an angular rate change of 0.0125 deg/s of the spacecraft. Figure 7 depicts the performance of the IPFM reaction jet controller designed to keep α_{atk} equal to $\alpha_{\text{atk},b}$. The control parameters correspond to a limit-cycle attitude θ_L equal to 1 deg and the damping coefficient ζ_c of an equivalent linear controller equal to 0.707. Figure 7 shows that the angle-of-attack α_{atk}, starting from zero, is brought close to $\alpha_{\text{atk},b}$, equal to 3.15 deg. It further shows that the pitch angle α_2

becomes approximately equal to $\alpha_{atk,b} + \xi$, and that the pitch rate $\dot{\alpha}_2$ tracks $\dot{\xi}$. In view of the constraints of given thruster parameters, the performance of the controller is thus very satisfactory. Reference 3 may be reviewed for further details.

V. Soft Martian Landing Controller

When a spin-stabilized interplanetary spacecraft approaches Mars, it is despun and, as Martian atmosphere becomes palpable, the tucked-in parachute is deployed, reducing the approach velocity to a constant terminal velocity, say 80 m/s, with possibly a sizable local horizontal component. The parachute is jettisoned at an altitude as low as the thrusters onboard and landing dynamics would permit, and both horizontal and vertical velocity components are reduced to almost zero by an active landing controller in the remaining altitude before touchdown. The controllers developed here accomplish this purpose and are significantly enhanced versions of the classical longitudinal and lateral controllers[9,10] for lunar landing.

A. Longitudinal Controller

The objective of this controller is to reduce the vertical velocity at the time of parachute jettisoning (a′, Fig. 8) to a specified, low, constant velocity v_c (1 m/s) by a certain altitude h_c (5 m, point b, Fig. 8) above the destination planet surface. An additional objective of the controller is to lower the spacecraft at a constant velocity from the point b to touchdown. In Refs. 9 and 10, the controller is turned off at a slight altitude (point c, Fig. 8), e.g., 1 m, to avoid raising dust with thruster plume and thereby contaminating the planetary surface. However, this requires an accurate altimeter to detect the point c, escalating the spacecraft cost and weight. The alternative adopted here is to let the controller bring the spacecraft down at a constant velocity until touchdown, whereupon the inertial reference unit (IRU) indicates zero vertical velocity and the controller then will turn itself off. The nominal free-fall phase cd and the actual free-fall phase c′d′ hence do not exist in the present controller.

Figure 9 (adapted from Fig. 13.12, p. 583, Ref. 10) depicts the geometry of descent. Let a_N be the nominal spacecraft deceleration

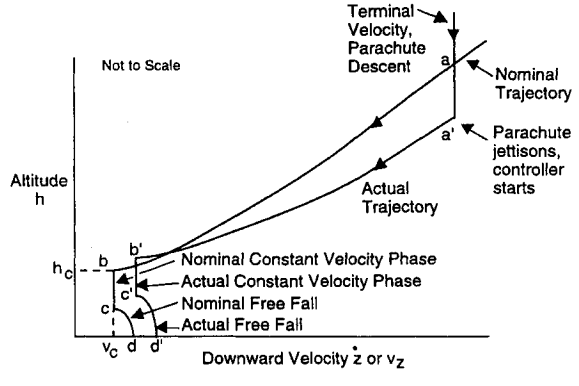

Fig. 8 Different phases of longitudinal motion in altitude and vertical velocity plane.

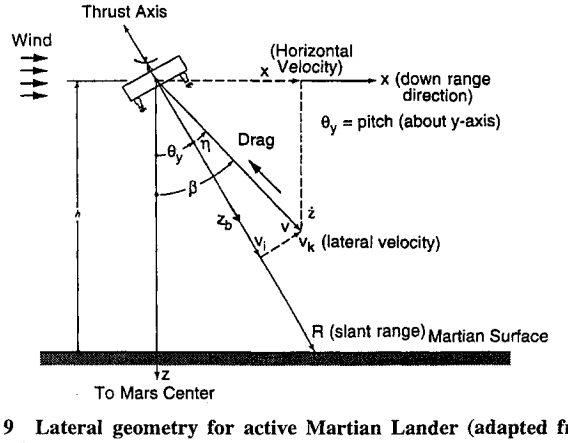

Fig. 9 Lateral geometry for active Martian Lander (adapted from Ref. 10).

in the body-fixed $-z_b$ direction produced by selected thrusters. Also, denote the Mars gravitational acceleration along the vertical z axis as g_M. Because the pitch angle θ_y is small, $|\theta_y| \ll 1$ rad, the net deceleration of the spacecraft along the z axis is essentially $(a_N - g_M)$. Because the spacecraft's reference trajectory passes through the point b (h_c, v_c) in the $h - v_z$ plane, Fig. 8, the commanded vertical velocity $\dot{z}_c$ at an altitude h must be

$$\dot{z}_c^2 = v_c^2 + 2(a_N - g_M)(h - h_c) \tag{26}$$

This provides a descent contour shown in the control block diagram, Fig. 10. The actual velocity $\dot{z}$, however, measured by a radar at the instantaneous spacecraft altitude or estimated by an IRU system, is usually different from $\dot{z}_c$. A noisy velocity error then is obtained as shown and filtered to arrive at a velocity error ε_v. To eliminate this error, the reference acceleration a_N is augmented by an incremental acceleration $K_a\varepsilon_v$ and the thrusters are turned on appropriately. A new velocity is measured or estimated again and the above procedure repeats itself. To determine a suitable value of the control gain K_a, note that the reference time T_0 required to bring the initial vertical velocity $\dot{z}_0$ to v_c is $T_0 = (\dot{z}_0 - v_c)/(a_N - g_M)$. Reference 9 shows that the error δh between the actual altitude and the current reference altitude decreases exponentially and $K_a T_0 > 5$ is a suitable gain because $\exp(-5) = 0.0067$. The nominal deceleration a_N is determined from Eq. (26), knowing the initial velocity $\dot{z}_0$ and the nominal initial altitude $h_{i,\text{nom}}$ at which the landing controller is turned on:

$$a_N = \frac{\dot{z}_0^2 - v_c^2}{2(h_{i,\text{nom}} - h_c)} + g_M \tag{27}$$

This is the minimum deceleration that the thrusters must supply. If they deliver more, their width is modulated so as to track a_N with little error.

The above controller is used also for the constant-velocity phase bc (Fig. 8) executed near ground. This phase is introduced because, otherwise, the lateral controller, discussed below, causes large pitch rate and pitch acceleration commands near the landing site. To effect a constant-velocity descent, the nominal acceleration a_N is set equal to g_M in the descent contour (26) when the measured altitude h (with measurement errors) is less than or equal to the specified altitude h_c (e.g., 5 m). Also, the nominal duration $t_{cv} = h_c/v_c$ of the constant-velocity phase is smaller than the time duration T_0 and therefore the acceleration gain K_a for this phase is set to be much larger than what $K_a t_{cv} = 5$ would allow.

B. Lateral Controller

The objective of this controller is to reduce to zero the initial horizontal velocity of the spacecraft using the same thrusters that concurrently decelerate the lander in the vertical direction. Consequently, the lander must be pitched for lateral control by an angle θ_y (Fig. 9), not necessarily the same as the angle β—the angle of the velocity vector with the vertical. When the pitch angle θ_y is equal to β, that results in gravity turn—a lateral control scheme with certain advantages elucidated and utilized subsequently. The block diagram of the lateral controller is shown in Fig. 11. It is an amended version of the controller in Fig. 13.13 of Ref. 10 wherein the commanded pitch rate $\dot{\theta}_{yc}$ is proportional to v_k/R, where v_k is the lateral velocity and R is the slant range (Fig. 9). Though $\dot{\theta}_{yc}$ so calculated is effective initially, the scheme slowly degrades inasmuch as it causes the spacecraft to swing while approaching the ground, with $\dot{\theta}_{yc}$ exhibiting divergent oscillations. Because this is unsatisfactory, $\dot{\theta}_{yc}$ is calculated instead from a suitable altitude downward (40 m presently) according to gravity turn, as portrayed in Fig. 11. The advantage of doing so is that the divergent oscillations in the pitch-rate command then are replaced by stable, smooth commands. The pitch command for gravity turn, in the linear regime, is $\theta_{yc} \approx \dot{x}/\dot{z}$. But even the gravity turn has its limitations because, as the spacecraft reaches very near the ground, both lateral and longitudinal velocity components approach zero and the rate and acceleration commands ($\dot{\theta}_{yc}$ and $\ddot{\theta}_{yc}$) become intolerably large. The lateral controller therefore is turned off altogether when $|\dot{x}| \leq 0.1$ m/s, accepting the residual small pitch angle and rate, and residual lateral velocity (1–1.5 m/s) and longitudinal velocity (0.5–2 m/s) to be withstood by the spacecraft structure and the resident electronic components.

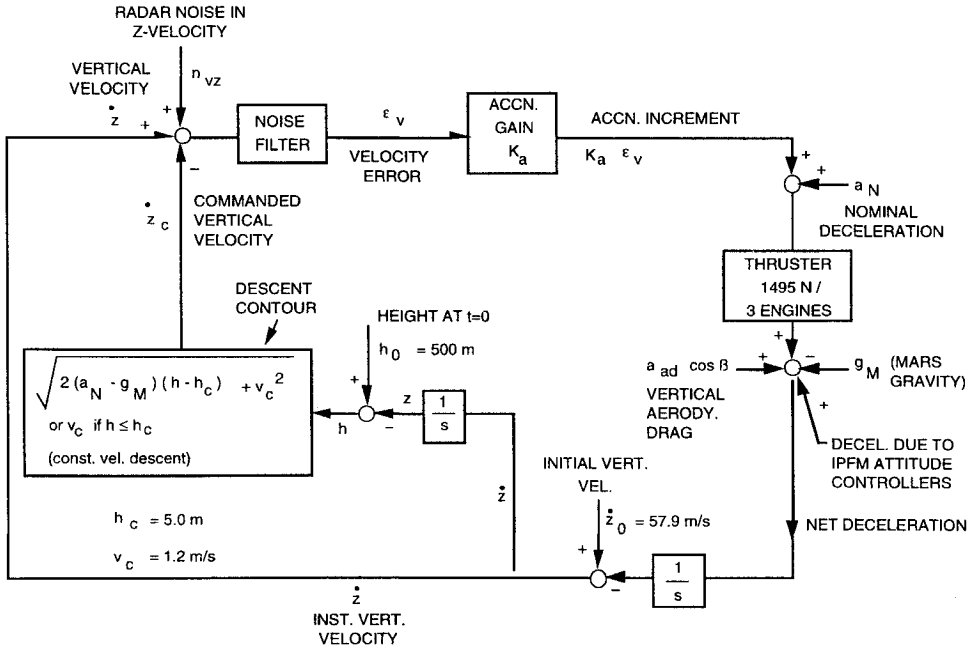

Fig. 10 Closed-loop longitudinal velocity controller.

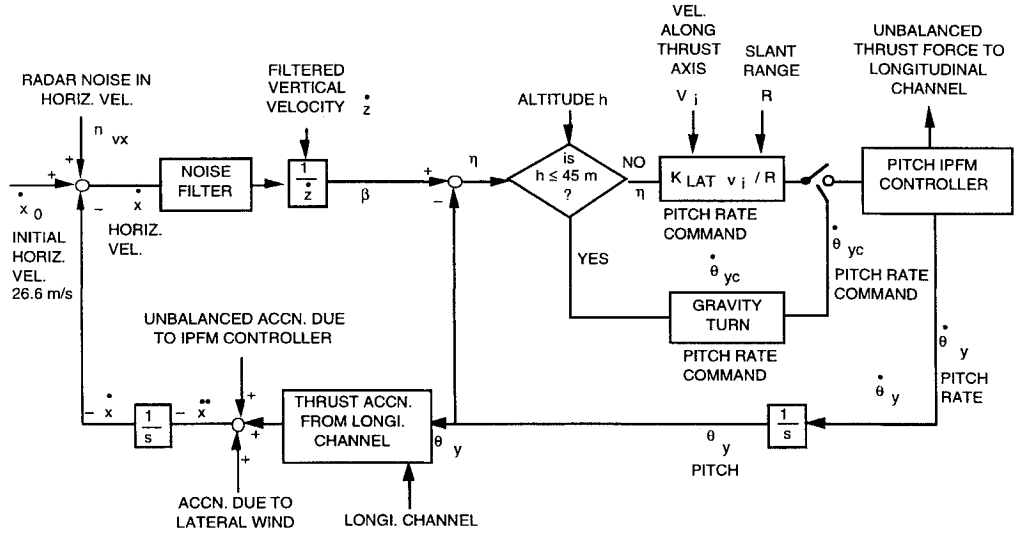

β, η = Lateral Geometry Angles; v_i defined in Lateral Geometry (Fig. 10)

Fig. 11 Lateral velocity controller for active Martian Lander.

Also, these touchdown conditions and the center of gravity of the lander are stipulated to be such that the lander does not overturn.

Regarding the gain K_{lat} in Fig. 11, the pitch rate command $\dot{\theta}_{yc}$ in linear regime (that is, small lateral velocity compared to the longitudinal velocity and small pitch angle), according to Pfeffer,[10] is $\dot{\theta}_{yc} = K_{\text{lat}}\eta v_i/R$, where the angle η and the longitudinal velocity v_i are defined in Fig. 9. The gain K_{lat} is optimal when it renders the two roots of the quadratic equation (13.52) of Ref. 10 equal, leading to

$$K_{\text{lat}} = \frac{(b_n - 1) \pm \left(b_n^2 - 2b_n\right)^{\frac{1}{2}}}{2} \tag{28}$$

where the positive constant b_n is defined as $b_n = 2a_N/(a_N - g_M) > 2$. Because the plus sign yields larger K_{lat} than the minus sign does, we adopt the plus sign and the larger gain.

In a gravity turn, the angle η (Fig. 9) is zero by definition and the commanded pitch angle θ_{yc} varies continuously as the horizontal and vertical velocity components $\dot{x}$ and $\dot{z}$ decrease and the spacecraft descends to the Martian surface. Knowing $\dot{x}$ and $\dot{z}$ with the aid of a radar or IRU, the ideal angle θ_{yc}, rate $\dot{\theta}_{yc}$, and acceleration $\ddot{\theta}_{yc}$ can be calculated to control the pitch attitude. This scheme therefore is used below a certain altitude, e.g., 40 m (Fig. 11), replacing the earlier problematic pitch-rate command.

Defining a quantity $\alpha_J = b_n/2$ (J for jets), the linear pitch command is found to be[3]

$$\theta_{yc} = \frac{\dot{x}_i \dot{z}^{\alpha_J - 1}}{\dot{z}_i^{\alpha_J}} = \frac{\dot{x}}{\dot{z}} \tag{29}$$

where $\dot{x}_i$ and $\dot{z}_i$ are the initial velocity components at the instant when the gravity turn is initiated. The pitch rate and acceleration commands are derived by differentiating θ_{yc} and substituting $\ddot{z} = -a_N + g_M$, arriving at

$$\dot{\theta}_{yc} = \frac{-g_M \dot{x}_i \dot{z}^{\alpha_J - 2}}{\dot{z}_i^{\alpha_J}} = \frac{-g_M \dot{x}}{\dot{z}^2} \tag{30}$$

$$\ddot{\theta}_{yc} = \frac{g_M(2g_M - a_N)\dot{x}_i \dot{z}^{\alpha_J - 3}}{\dot{z}_i^{\alpha_J}} = \frac{g_M(2g_M - a_N)\dot{x}}{\dot{z}^3} \tag{31}$$

Comparing $I_2\ddot{\theta}_{yc}$ (I_2 = pitch moment of inertia) with the available pitch-control torque, the gravity turn can be terminated when the former exceeds the latter, and the constant velocity descent then begins.

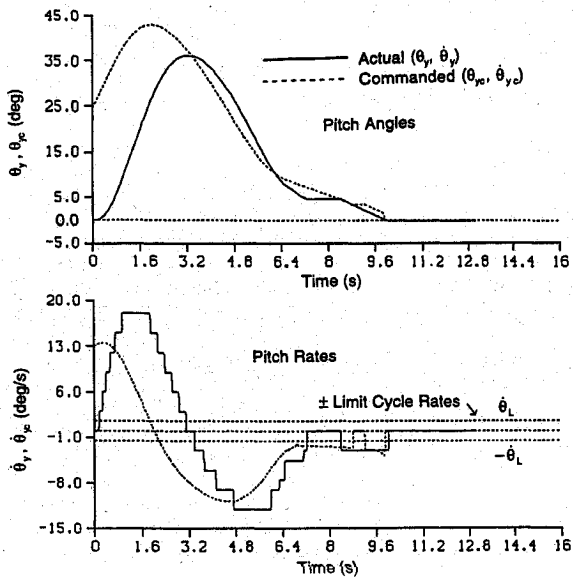

Fig. 12 Pitch and pitch-rate control: actual and commanded.

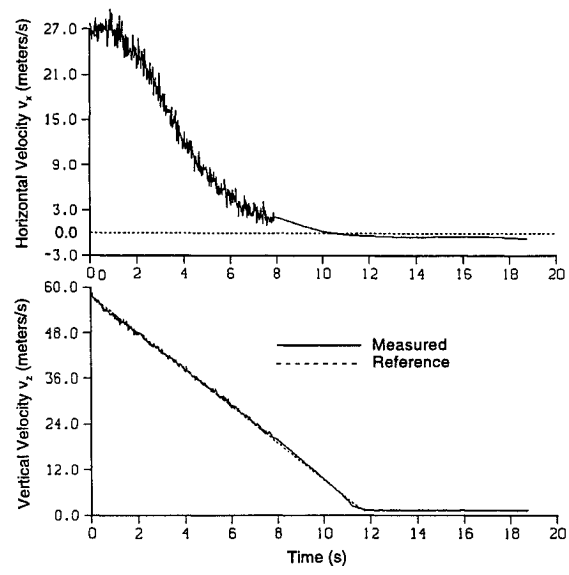

Fig. 13 Performance of a soft landing controller with a noisy radar altimeter above 45 m, a noiseless IRU below 45 m, and a digital noise filter: horizontal and vertical velocity components.

C. Numerical Results

The performances of increasingly more complete landing controllers were examined and extensive simulation studies were conducted but, to conserve space, only limited results are shown here.

Reference 3 illustrates an unsatisfactory, oscillatory pitch-control performance of the original landing controller of Refs. 9 and 10 without gravity turn for pitch control at low altitudes. Figure 12, in contrast, illustrates performance of the pitch controller when the gravity turn is incorporated below 45-m altitude, provided the horizontal velocity magnitude $|v_x|$ is greater than 0.1 m/s. The unacceptable divergent oscillations are absent in Fig. 12 because 1) when $h <$ 45 m and $|v_x| > 0.1$ m/s, the smooth pitch and pitch rate commands are obtained from Eqs. (29) and (30); 2) when the horizontal velocity $|v_x| \leq 0.1$ m/s, regardless of the altitude, the commanded pitch angle and the rate ω_{yc} are both zeroed; and 3) the pitch angle and rate commands are both zeroed in the constant-velocity phase below 5 m.

The performance of the landing controller which, in addition to gravity turn, uses a radar altimeter with certain measurement noise characteristics and digital fading memory filters to smooth noisy altitude and velocity measurements is illustrated in Figs. 13 and 14. Because of excessive noise in the measurements below 45-m altitude, the radar altimeter is cut off at 45 m and IRU navigation of the lander is initialized with the last measurement of the velocity and altitude by the radar assembly. Although the altitude measurements have random errors, they are not modeled here; only their bias error is modeled. At 45-m altitude, the IRU inherits a bias altitude error of -2.14 m (2.58σ value to include 95% error probability) of the altimeter. A positive-bias velocity error and a negative-bias altitude error are chosen for illustration because the actual velocity then is less and the actual altitude is more than the quantities measured. Consequently, the lander takes longer to touch the ground than the reference constant-velocity duration, t_{cv}, yielding an estimate of the required worst propellant consumption. Moreover, 1σ value of the random velocity noise is not constant (noise is nonstationary); it is instead proportional to velocity.[1/2]

Figures 13 and 14 illustrate a sample performance of the multiaxis landing controller amidst velocity and altitude noise, filtered by a first-order filter, the coefficients of which are selected according to its optimum stochastic response to noise and its rise time. The initial altitude in these figures is set at 348.84 m, based on a reference altitude of 350 m and a 1.66% 1σ bias error in altitude measurements. The actual and reference vertical velocity profiles (Fig. 13) confirm the earlier conclusion that, because of a negative altitude bias error of -2.14 m and a positive vertical velocity bias error of 0.48 m/s, the actual touchdown takes longer than the reference touchdown (nearly 19 s vs 15.85 s). The vertical touchdown velocity is about 1.2 m/s—the constant velocity of the final descent. Also, because the horizontal velocity bias error is positive (0.8 m/s),

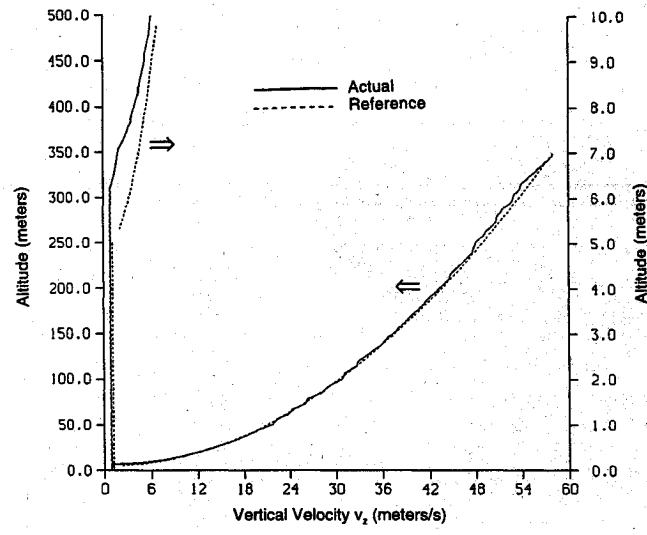

Fig. 14 Altitude vs vertical velocity v_z: comparison of actual and reference trajectories.

the actual touchdown horizontal velocity v_x is negative, -1.32 m/s (Fig. 13). Because the IRU navigation system operates essentially noise-free below $h = 45$ m, the velocities are seen to be such after $t = 8$ s, where the lander crosses 45-m altitude. The $h - v_z$ guidance trajectory and actual trajectory are portrayed in Fig. 14, where we observe that the longitudinal controller tracks the guidance trajectory easily during both the constant-acceleration phase and the constant-velocity phase, the latter starting at a true altitude of $5 + 2.14 = 7.14$ m instead of 5 m due to -2.14 m of h_{bias} error. Figure 28 in Ref. 3 shows picturesquely the poignant descent of the lander in the altitude-downrange plane. Therein enthralling is its slight horizontal backward motion just before touchdown, preening with pride.

VI. Concluding Remarks

Four attitude controllers are presented for spinning and nonspinning phases of interplanetary spacecraft. For Rhumb-line precession of the spin axis, it is crucial to maintain a constant phase of thruster pulses with the sun. To meet this condition, these pulses must be slightly aperiodic; exactly periodic pulses at spin period would veer the spin axis to an unintended direction. Thrusters can damp very effectively nutations of spacecraft with products of inertia if its transverse angular rates are passed through suitably designed bandpass filters that eliminate constant rate biases. When the spacecraft arrives at the destination planet, the initial highly eccentric orbit

is circularized with aerobraking. Attitude of the spacecraft can be controlled during aerobraking, amid an order-of-magnitude uncertainty in the air density, with IPFM reaction jet controller, provided the reference pitch and pitch-rate commands are inputted to the controller. Finally, the vertical and horizontal velocity controllers available in the literature for soft landing are inadequate because the latter controller causes divergent oscillations in pitch and pitch-rate commands as the spacecraft approaches the ground. This shortcoming is removed by switching at a suitable intermediate altitude, e.g., 50 m, to pitch and pitch-rate commands associated with gravity turn. When very close to the ground, e.g., 5-m altitude, a constant-velocity reference trajectory is introduced in the vertical velocity controller for a soft touchdown of the spacecraft.

Acknowledgment

With great pleasure, I wish to acknowledge my numerous insightful technical discussions, over the years, with the Guidance, Navigation, and Control Lead Engineer A. Cormack. Without his guidance, it is inconceivable how these efforts would have been brought to fruition.

References

[1]Greene, R. H., "Early Bird Placement in a Stationary Orbit: Launch and Control System Maneuvers," AIAA Paper 66-262, May 1966.

[2]Furukawa, M., "Precession Maneuver Performed by Applying a Uniform Train of Thrust Pulses," *Journal of Spacecraft and Rockets*, Vol. 13, No. 10, 1976, pp. 600–604.

[3]Hablani, H. B., "Interplanetary Spacecraft Controllers Using Thrusters," *AIAA Guidance, Navigation, and Control Conference*, AIAA, Reston, VA, 1997, pp. 1590–1612 (AIAA Paper 97-3754).

[4]Wertz, J. R., *Spacecraft Attitude Determination and Control*, Reidel, Boston, MA, 1984, pp. 649–654.

[5]Devey, W. J., Field, C. F., and Flook, L., "An Active Nutation Control System for Spin Stabilized Satellites," *Proceedings of 6th IFAC Triennial World Congress* (Boston/Cambridge, MA), 1975, pp. 14.1/1–10.

[6]Carpenter, A. S., "The Magellan Aerobraking Experiment: Attitude Control Simulation and Preliminary Flight Results," *AIAA Guidance, Navigation, and Control Conference*, AIAA, Washington, DC, 1993, pp. 1148–1158 (AIAA Paper 93-3830).

[7]Carpenter, A. S., and Dukes, E., "Control of the Magellan Spacecraft During Atmospheric Drag," American Astronautical Society, 17th Annual AAS Guidance and Control Conf., Paper 94-064, Keystone, CO, Feb. 1994.

[8]Hablani, H. B., "Target Acquisition, Tracking, Spacecraft Attitude Control, and Vibration Suppression with IPFM Reaction Jet Controllers," *Journal of Guidance, Control, and Dynamics*, Vol. 17, No. 4, 1994, pp. 831–839.

[9]Cheng, R. K., and Pfeffer, I., "Terminal Guidance System for Soft Lunar Landing," *Guidance and Control*, edited by R. E. Roberson and J. S. Farrior, Vol. 8, Progress in Astronautics and Rocketry, Academic, New York, 1962, pp. 217–239.

[10]Pfeffer, I., "Terminal Guidance for Soft Lunar Landing," *Guidance and Control of Aerospace Vehicles*, edited by C. T. Leondes, McGraw–Hill, New York, 1963, pp. 563–587.